An Automated Monitoring Strategy for Ultrasonic Amplitude Prediction of Piezoelectric Transducer

Heng Zhao[1], Jianzhong Ju[1], Shuyuan Ye[1], Xuan Li[2], Zhili Long[1]*

[1]*Department of Mechanical Engineering and Automation, Harbin Institute of Technology (Shenzhen), Shenzhen, China*
[2]*Centre for Medical and Industrial Ultrasonics, (C-MIU), James Watt School of Engineering, University of Glasgow, Glasgow, G12 8QQ, U.K.*

Abstract： Piezoelectric transducer (PT) is the key component in power ultrasonics. Its vibration amplitude directly reflects the performance of the transducer. The real time measurement of amplitude is seldomly reported and difficult to be realized due to the high frequency and confined space to accommodate a sensor. Currently, there are no viable solutions for monitoring the amplitude when the tool is engaged in the material. We present a real time, low-cost amplitude monitoring strategy of the PT, incorporating voltage, current and resonant frequency. The piezoelectric and wave transmission equation are combined with the displacement and force boundaries. The displacement amplitude of the PT is predicted by the established numerical model based on the voltage, current and resonant frequency. Validating experiments are conducted and experimental results demonstrate that the amplitude measurements have a good agreement with the mathematic simulation, which has confirmed the validity of the proposed technique.
Key words: Amplitude prediction; Real-time monitoring; Piezoelectric transducer; Piezoelectric equation; Wave equation.

1. Introduction

A piezoelectric transducer (PT), which converts electrical power into mechanical vibration in high frequency (more than 15 kHz), is the key component in power ultrasonic systems [1, 2]. Currently, PTs are being widely used in various industrial processes, such as rotary ultrasonic machining (RUM), ultrasonic plastic soldering (UPS), and wire bonding (WB). RUM is an efficient material removal process which has been proved to improve the machining efficiency and the surface roughness of the workpiece by using the 20~40 kHz ultrasonic energy [3-7]. UPS can achieve material formation and fabrication in a higher efficiency compared to the traditional process [8]. WB is an advanced technology of fine-pitch package for the microelectronics devices, where with a frequency higher than 55 kHz can achieve the bonding connections in a faster and greener manufacturing [9-12]. These examples show that the vibration amplitude of the PT is of great significance to promote the efficiency, quality and uniformity of the machining processes [13-15]. Moreover, the vibration amplitude is affected due to the constantly changing force and thermal effects during the fabrication process [16-17]. Therefore, it is necessary to monitor the vibration amplitude of the PT when the force is present.

In order to measure the displacement amplitude of the PT, Laser Doppler Vibrometer (LDV) apparatus is widely used. Many researchers choose to use this optic sensors and data acquisition systems (Polytech or KEYENCE) to measure the vibration amplitude. However, the optical method is unsuitable for collecting vibration samples in real time in harsh working environment, as well as in a confined space, such as in water, fog, smog and tool tip when engaged with the material [18]. Moreover, this expensive testing method has a limited access in industrial application. In academic, Zhou et al. proposed the amplitude prediction method of a giant magnetostrictive ultrasonic transducer [19,20]. It is noted that the model must be performed for any giant magnetostrictive ultrasonic transducer and this method is not adapted to the PT. Gaul et al. discovered that, in the ultrasonic wedge/wedge bonding, the transversal force is related to the amplitude of the tool [21]. The predicted amplitude must be calibrated by additional experiments. Cong and M. A. Moghaddas proposed an amplitude measurement method by using the microscope to observe the machined surface due to the marks caused by the cutting tool [22, 23]. The microscopic measurement is done off-line and is only applied to plastic materials, which demonstrated a low precision. Saber et al. proposed a model to predict the vibration amplitude of high-power PT by using temperature measured by a thermo-couple and estimated the power transmission to the air [24, 25]. The downsides of this model are the high dependence on the environment, and low accuracy of complicated heat dissipation. Ning et al. established a mechanistic amplitude model through cutting force of brittle materials [26]. The major limitation of this model is the high-cost of the dynamometer, and the errors caused by the cutting force are not discussed in the investigation. Therefore, developing an accurate PT vibration amplitude prediction model that can work in real time machining process under harsh working environment is beneficial to better understand the tool-workpiece interaction mechanism.

In recent years, many scholars are dedicated for the investigations on the dynamic characteristics of the

PTs to monitor the vibration amplitude. S. Voronina et al. proposed an auto-resonant control strategy to maintain the amplitude under loaded machining applications [27]. Mohammad Reza Karafi et al. presented the kinematic equations by solving wave equations with displacement and force continuous boundary conditions [28]. The vibration displacement correlated with the ultrasonic amplitude and the piezoelectric stack are established, but the displacement of PZT stack with current/voltage is not involved. Zhao et al. studied the stability of longitudinal-torsional rotary ultrasonic transducer considering load effects [29, 30]. The transfer matrix of wave equation based on the piezoelectric equation is combined to derive the relationship between current, impedance and amplitude. It is mentioned that vibration displacement of the piezoelectric stack is transmitted to the front solid horn. Actually, the vibration displacement of the piezoelectric stack is transferred to both side of the PT.

Ultrasonic amplitude of PT is the critical parameter in determining fabrication performance of an ultrasonic transducer. However, investigations on all of the reported methods suggest that no viable solution are suitable for real-time monitoring amplitude in a confined space to accommodate a sensor, such as in water, fog, smog and tool tip when engaged with the material. In this study, we present a novel amplitude prediction strategy that is suitable for PT amplitude real-time monitoring in idle and load conditions. The vibration amplitude can be monitored with self-developed ultrasonic generator and predicted by using the voltage, current and resonant frequency with a theoretical model. Three PTs, namely RUM, UPS and WB are used in experiments. Results show that the predicted vibration amplitude using voltage, current and resonant frequency are consistent with the measurements.

2. Analytical model

Fig. 1 presents a typical bolted Langevin-style PT, which consists of a back slab and a front solid horn, sandwiching a stack of piezoceramic rings by a pre-stress bolt. A tool is attached to the solid horn to ensure the BLT is operated on the material processing, and one of the longitudinal displacement nodal is located at the flange where can be clamped with an external fixture to minimize the energy loss. For any constant rod of the transducer in Fig.1, lengths and cross-sectional areas of the sections of the BLT components are represented in l_i and S_i; and the right end is set to x_i=0 and the left end is set to x_i=l_i (i=1, 2, …, 6).

2.1 Flow chart of displacement prediction

Fig. 2 shows the flow chart to predict the amplitude of a PT, which is calculated based on a model that is deduced by combining piezoelectric and wave propagation equations. Based on the piezoelectric equation, the relationship between the displacement, voltage/current, and frequency is derived. The displacement transmission equation of the PZT stack, horn, and tool is deduced using the wave propagation equation. Then, the vibration amplitude of tool tip at the operating resonant frequency with voltage/current is realized according to the displacement and force continuous boundary conditions.

2.2 Dynamic displacement of the PZT stack

The strain-charge form of the piezoelectric effect of the piezoelectric elements of the PT is described as follows:

$$\begin{cases} T = c^E S_p - e_p E_p \\ D = e_p S_p + \varepsilon_p E_p \end{cases} \tag{1}$$

Where, T is the stress, D is the dielectric displacement; c^E is acoustic propagation speed; S_p is the strain; e_p is the piezoelectric constant; E_p is the applied electric field strength; ε_p is the dielectric constant. The piezoelectric ceramics used in this study is PZT-4 [30], and the material parameters are listed in Table 1. The physical parameters in equation (1) also satisfy the relationships as follows [25]:

$$T = \frac{F_T}{S_5},\ E_p = \frac{u}{l_5},\ S_p = \frac{x_0}{l_5},\ D = \frac{q}{S_5},\ I = 2\pi f q \tag{2}$$

Where, F_T is the integrating load due to deformation and externally applied force; S_5 is the cross-sectional area of PZT stack; u is the applied voltage; l_5 is the length of PZT stack; x_0 is the displacement of PZT stack;

Table 1
Parameters of PZT-4

Type	Parameters	Value
Density	ρ_{pzt}	7500kg/m^3
Elastic modulus	E_{pzt}	64.5Gpa
Piezoelectric constant	e_p	15.1Cm^{-2}
Dielectric constant	ε_p	1300×8.8541878×10^{-12}F/m

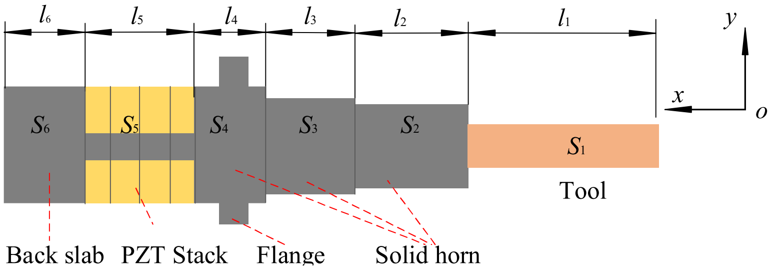

Fig.1. Piezoelectric ultrasonic transducer.

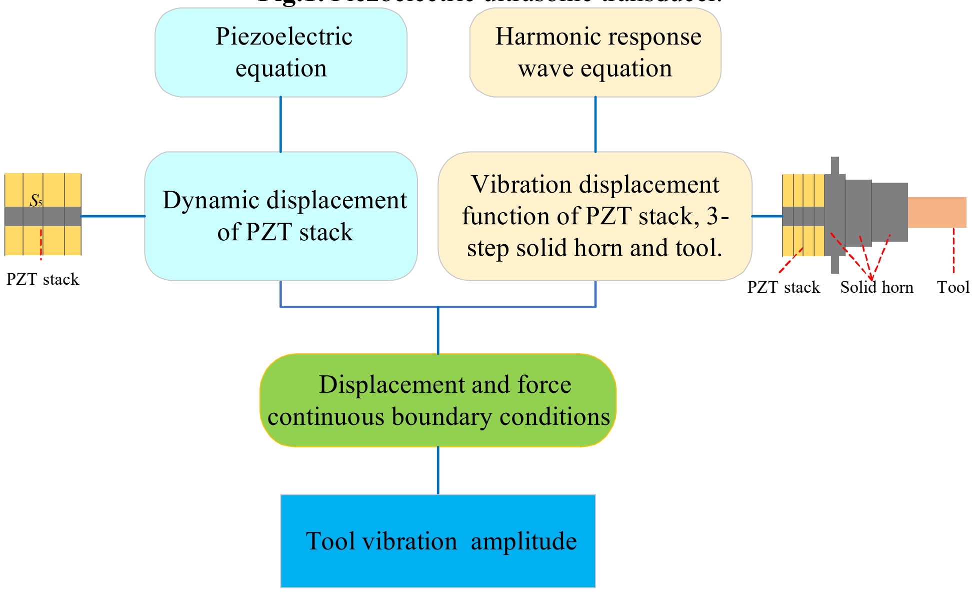

Fig.2. Flow chart of displacement prediction.

q is the charge; I is the corresponding current of charge q as the ultrasonic transducer is operated at harmonic resonance; f is the resonant frequency. Thus, the piezoelectric equation is deduced as:

$$\begin{cases} \dfrac{F_T}{S_5} = \dfrac{c^E}{l_5} x_0 - \dfrac{e_p}{l_5} u \\ \dfrac{I}{S_5} = \dfrac{2\pi f e_p}{l_5} x_0 + \dfrac{2\pi f \varepsilon_p}{l_5} u \end{cases} \tag{3}$$

The piezoelectric equation consists of mechanical branch and electrical branch, among which correlates with each other by the displacement x_0 and the externally applied voltage u. In equation (3), the current I that involves with the displacement x_0 and the applied voltage u is just considered in the amplitude prediction model. Thus, the displacement x_0 on the PZT stack can be expressed as follows:

$$x_0 = \frac{l_5}{2\pi f e_p S_5} I - \frac{\varepsilon_p}{e_p} u \tag{4}$$

The displacement expression suggests that the amplitude of the PZT stack can be calculated if the voltage, current and frequency are available as the geometric dimension and material characteristics of the PZT-4 stack are determined.

2.3 Vibration transmission equation of PT

As the cross-sectional area of the PT is smaller than the 1/4 wavelength of the transducer, the wave equation of the PT vibrating in harmonic one-dimensional longitudinal state can be expressed as [31-33]:

$$\frac{\partial^2 d_i}{\partial x_i^2} + k_i^2 d_i = 0 \tag{5}$$

Where, x_i is the location of constant rod; d_i is vibration displacement at location x_i; $k_i = 2\pi f / c_i$ is wave constant; $c_i = \sqrt{E_i / \rho_i}$ is the sound velocity in the material; E_i is the material elastic modulus; ρ_i is the horn material density. The displacement expressions of different parts in Fig. 1 are solved as:

$$d_i(x_i) = A_{i1} \cos(k_i x_i) + A_{i2} \sin(k_i x_i), i = 1,2,3,4,5,6 \tag{6}$$

Where, A_{i1} and A_{i2} are the constant displacement coefficient of each rod. The displacement and force continuous boundary condition of rod $l_1 \sim l_5$ at the adjacent border is as follows:

$$\begin{cases} d_i(0) = d_{i\text{-}1}(l_{i\text{-}1}) \\ E_i S_i \dfrac{\partial d_i(0)}{\partial x_i} = E_{i\text{-}1} S_{i\text{-}1} \dfrac{\partial d_{i\text{-}1}(l_{i\text{-}1})}{\partial x_{i\text{-}1}} \end{cases} \tag{7}$$

Where, E_i is the elastic modulus of each rod; S_i is the area of each rod. By applying the displacement and force continuous boundary conditions, the displacement equation of the coefficients A_{i1} and A_{i2} of $l_1 \sim l_5$ can be deduced as:

$$\begin{cases} A_{21} = A_{11}\cos(k_1l_1) + A_{12}\sin(k_1l_1) \\ E_2S_2k_2A_{22} = E_1S_1k_1[-A_{11}\sin(k_1l_1) + A_{12}\cos(k_1l_1)] \\ A_{31} = A_{21}\cos(k_2l_2) + A_{22}\sin(k_2l_2) \\ E_3S_3k_3A_{32} = E_2S_2k_2[-A_{21}\sin(k_2l_2) + A_{22}\cos(k_2l_2)] \\ A_{41} = A_{31}\cos(k_3l_3) + A_{32}\sin(k_3l_3) \\ E_4S_4k_4A_{42} = E_3S_3k_3[-A_{31}\sin(k_3l_3) + A_{32}\cos(k_3l_3)] \\ A_{51} = A_{41}\cos(k_4l_4) + A_{42}\sin(k_4l_4) \\ E_5S_5k_5A_{52} = E_4S_4k_4[-A_{41}\sin(k_4l_4) + A_{42}\cos(k_4l_4)] \end{cases} \quad (8)$$

Furthermore, the above displacement equations can be turned into the matrix equation $[A_{j1}\ A_{j2}]^T$ as:

$$\begin{bmatrix} A_{j1} \\ A_{j2} \end{bmatrix} = T_i \begin{bmatrix} A_{i1} \\ A_{i2} \end{bmatrix}, T_i = \begin{bmatrix} T_i^1 & T_i^2 \\ T_i^3 & T_i^4 \end{bmatrix}$$

$$= \begin{bmatrix} \cos(k_il_i) & \sin(k_il_i) \\ -\dfrac{E_iS_ik_i}{E_jS_jk_j}\sin(k_il_i) & \dfrac{E_iS_ik_i}{E_jS_jk_j}\cos(k_il_i) \end{bmatrix}, j = i+1 \quad (9)$$

Where T_i is the matrix of the transmission relationship from i-th rod to next adjacent $j(j=i+1)$-th rod. The overall transmission matrix from tool end to PZT stack can be obtained as:

$$\begin{bmatrix} A_{51} \\ A_{52} \end{bmatrix} = T[\begin{matrix} A_{11} \\ A_{12} \end{matrix}],\ T = T_4T_3T_2T_1 = \begin{bmatrix} T_a & T_b \\ T_c & T_d \end{bmatrix} \quad (10)$$

2.4 Vibration amplitude prediction model

As the initial vibration of the PZT stack is derived, the displacement of tool end can be reversely deduced by the displacement and force continuous boundary conditions. Particularly, we can get the displacement function of constant tool l_1:

$$d_1(x_1) = A_{11}\cos(k_1x_1) + A_{12}\sin(k_1x_1) \quad (11)$$

By using similar principle of [28], let $x_1 = 0$ and we can get:

$$d_1(0) = A_{11} \quad (12)$$

It can be seen from (12) that $A\_predicted=|A_{11}|$ is the tool end displacement and also the tool constant rod l_1 maximum amplitude in harmonic state. On the other hand, the displacement function of l_1 can be presented as:

$$d_1(x_1) = \sqrt{{A_{11}}^2 + {A_{12}}^2}\cos(k_1x_1 - \beta), \beta = \arctan(\frac{A_{12}}{A_{11}}) \quad (13)$$

It should meet the requirement of

$$\sqrt{{A_{11}}^2 + {A_{12}}^2} \le \sqrt{{A_{11}}^2} \quad (14)$$

From this equation, we can obtain that A_{12}=0. On the other word, the displacement coefficient A_{i1} and A_{i2} of (8) and (10) can be calculated in terms of A_{11}. Thus, the coefficient of A_{51} and A_{52} are expressed as follows:

$$\begin{bmatrix} A_{51} \\ A_{52} \end{bmatrix} = \begin{bmatrix} T_a & T_b \\ T_c & T_d \end{bmatrix} [\begin{matrix} A_{11} \\ 0 \end{matrix}] \quad (15)$$

The displacement function of PZT stack can be presented by:

$$d_5(x_5) = A_{51}\cos(k_5x_5) + A_{52}\sin(k_5x_5) \quad (16)$$

As dynamic displacement of x_0 is the integrating both end displacement of PZT stack, it can be realized from (15) and (16) as:

$$\begin{cases} x_0 = d_5(x_5)|_{x_5=0} - d_5(x_5)|_{x_5=l_5} = A_{11}M \\ M = [T_a - T_a\cos(k_5l_5) - T_c\sin(k_5l_5)] \end{cases} \quad (17)$$

Thus, the amplitude expression at the tool tip of the PT is established by (4) and (17) as:

$$A\_predicted = |A_{11}| = |-A\_voltage + A\_current| \quad (18)$$

$$A\_voltage = \frac{\varepsilon_p}{e_pM}u \quad (19)$$

$$A\_current = \frac{l_5}{2\pi fe_pS_5M}I \quad (20)$$

The above amplitude prediction *A_predicted* involves the characteristic parameters such as geometric dimension (l_i, S_i), material properties (E_i, ρ_i, e_p), resonant frequency (f), voltage(u) and current (I). The *A_voltage* represents the effect of voltage on amplitude prediction and the *A_current* represents the effect of current on amplitude prediction. The resonant frequency of PTs can be determined using equivalent circuit method and finite element method (FEM) with specific materials property and geometric dimension [10, 34, 35].

3. Simulation analysis

Three types of PT prototypes as RUM, UPS and WB transducers shown in Fig. 3, are employed in the experiments to validate the amplitude prediction model. The dimensions and material properties of PTs are listed in Table 2. Based on the theoretical model (18), (19) and (20), we conducted a mathematical simulation for amplitude prediction, where the effects of electrical voltage, current on vibration amplitude are defined as *A_voltage*, *A_current*. The resonant frequency of RUM, UPS and WB in simulation are set to be 25.9kHz, 20kHz and 56.5kHz, respectively. The simulation result is presented in Fig.4. It can be seen that the vibration amplitude of *A_voltage* and *A_current* increases linearly with the elevating of voltage/current in defined frequency. It is obvious that the current makes more significant influences on the amplitude than the one of voltage. Therefore, we can conclude that the current effect of *A_current* can be regarded as the predicted amplitude *A_predicted*. The coefficient between the amplitude and the current of RUM, UPS and WB transducers are calculated as β_{RUM} = 0.0351 (μm/mA), β_{UPS} = 0.0221 (μm/mA), β_{WB} = 0.0109 (μm/mA).

It is known that the resonant frequency of transducer is changing by the voltage, temperature, or force loading. The effect of current and frequency on the amplitude is simulated and shown in Fig.5. It is also found that the amplitude turns high with the increasing of the current. For RUM and WB transducer, the amplitude reduces gradually when the resonant frequency turns up. For UPS transducer, the amplitude elevates as the frequency enhances. The result of Fig. 5

means that the vibration amplitude can be predicted when the driving frequency and current is determined.

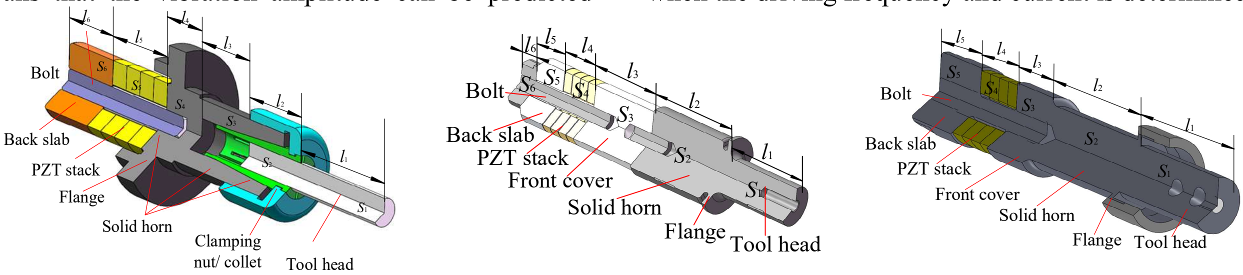

(a) RUM (b) UPS (c) WB

Fig.3. Geometry dimensions of transducers: (a)RUM, (b)UPS, (c)WB.

Table 2
Parameters of RUM, UPS and WB transducers.

Type	Geometric dimensions	Material properties
RUM	$l_1 = 20\text{mm};\ l_2 = 16\text{mm};\ l_3 = 16\text{mm};\ l_4 = 9.5\text{mm};$ $l_5 = 16\text{mm}; D_1 = 6\text{mm}; D_2 = 15\text{mm};\ D_{31} = 7.6\text{mm};$ $D_{32} = 15\text{mm}; D_4 = 15\text{mm}; D_{51} = 6\text{mm}; D_{52} = 15\text{mm}.$	$\rho_1 = \rho_2 = \rho_3 = \rho_4 = 7850\text{kg/m}^3;$ $\rho_5 = 7500\text{kg/m}^3;$ $E_1 = E_2 = E_3 = E_4 = 215\text{GPa};$ $E_5 = 64.5\text{GPa}.$
UPS	$l_1 = 60\text{mm};\ l_2 = 70\text{mm};\ l_3 = 48\text{mm}; l_4 = 28\text{mm};$ $D_1 = 31\text{mm};\ D_2 = 54\text{mm};\ D_3 = 50\text{mm};$ $D_{41} = 20\text{mm}; D_{42} = 50\text{mm}.$	$\rho_1 = \rho_2 = 7850\text{kg/m}^3;\ \rho_3 = 2730\text{kg/m}^3;$ $\rho_4 = 7500\text{kg/m}^3;\ E_1 = E_2 = 215\text{GPa};$ $E_3 = 71.7\text{GPa}; E_4 = 64.5\text{GPa}.$
WB	$l_1 = 26\text{mm};\ l_2 = 22\text{mm};\ l_3 = 10.2\text{mm}; l_4 = 9.2\text{mm};$ $D_1 = 9.5\text{mm};\ D_2 = 11.1\text{mm};\ D_3 = 13.5\text{mm};$ $D_{41} = 5\text{mm};\ D_{42} = 12.7\text{mm}.$	$\rho_1 = \rho_2 = \rho_3 = 7850\text{kg/m}^3;\ \rho_4 = 7500\text{kg/m}^3;$ $E_1 = E_2 = E_3 = 195\text{GPa}; E_4 = 64.5\text{GPa}.$

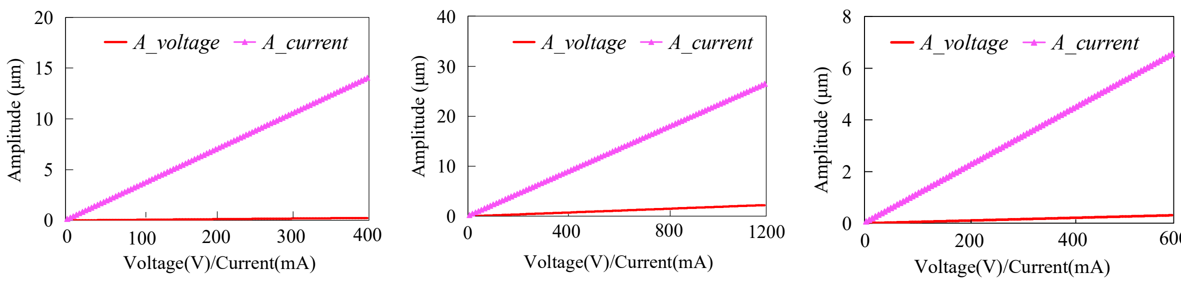

(a) RUM (b) UPS (c) WB

Fig.4. The effect of current and voltage on amplitude in simulation.

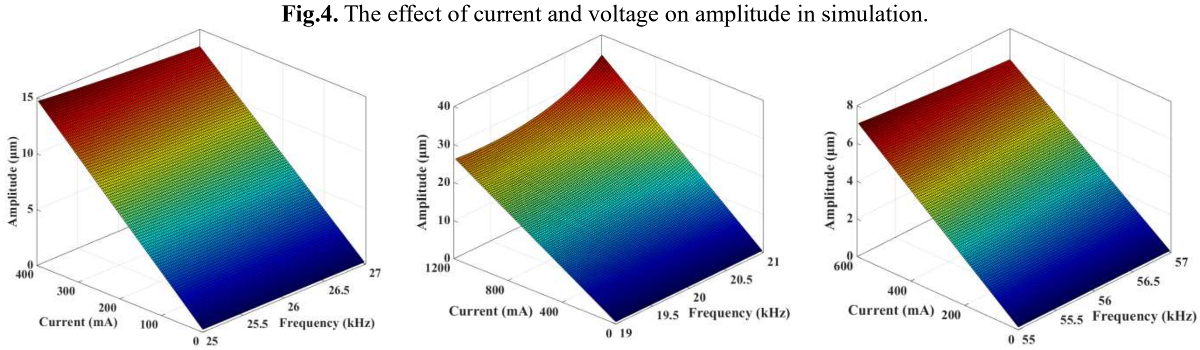

(a) RUM (b) UPS (c) WB

Fig.5. The effect of current and frequency on amplitude in simulation.

4. Experiments and discussion

4.1 Ultrasonic driving and automated monitoring system

The ultrasonic driving and automated monitoring system of voltage, current, frequency and amplitude is developed and used to trigger the PTs. Fig. 6 (a) shows the hardware schematic of the driving and control system. In our design, a micro controller unit (MCU) STM32F103 of Coretex-M3 with a 32-bit processing speed is selected to control all signals. As the control core unit of the driving system, this microcontroller unit (MCU) can meet the high speed, precision control such as signal generator, frequency tracking, and the communication to peripherals. The resonant frequency of ultrasonic transducer specified by MCU is determined by using the automatic sweep function to find the maximum admittance and corresponding initial phase in idle condition. The determined initial phase mode is used to tune the zero-phase impedance matching circuit of LC filter that make the matched phase is approaching zero [36-38]. Especially, the LC filter of impedance matching circuit and voltage sampling resistance is shown in Fig. 6 (b). Inductance L_1 and capacitors C_1, C_2, C_3 of appropriate quantity and magnitude based on the equivalent circuit parameter of ultrasonic transducer can be tuned to meet the requirement of different operating frequency that driving at approaching zero phase/impedance frequency. The resonant frequency is then tracked by the matched initial phase in long-time excitation. When the transducer vibrates at a frequency lower than the matched initial phase, an increased driving frequency is required. Conversely, if the transducer is excited in a higher frequency that the actual phase beyond the matched initial phase, the exciting frequency is

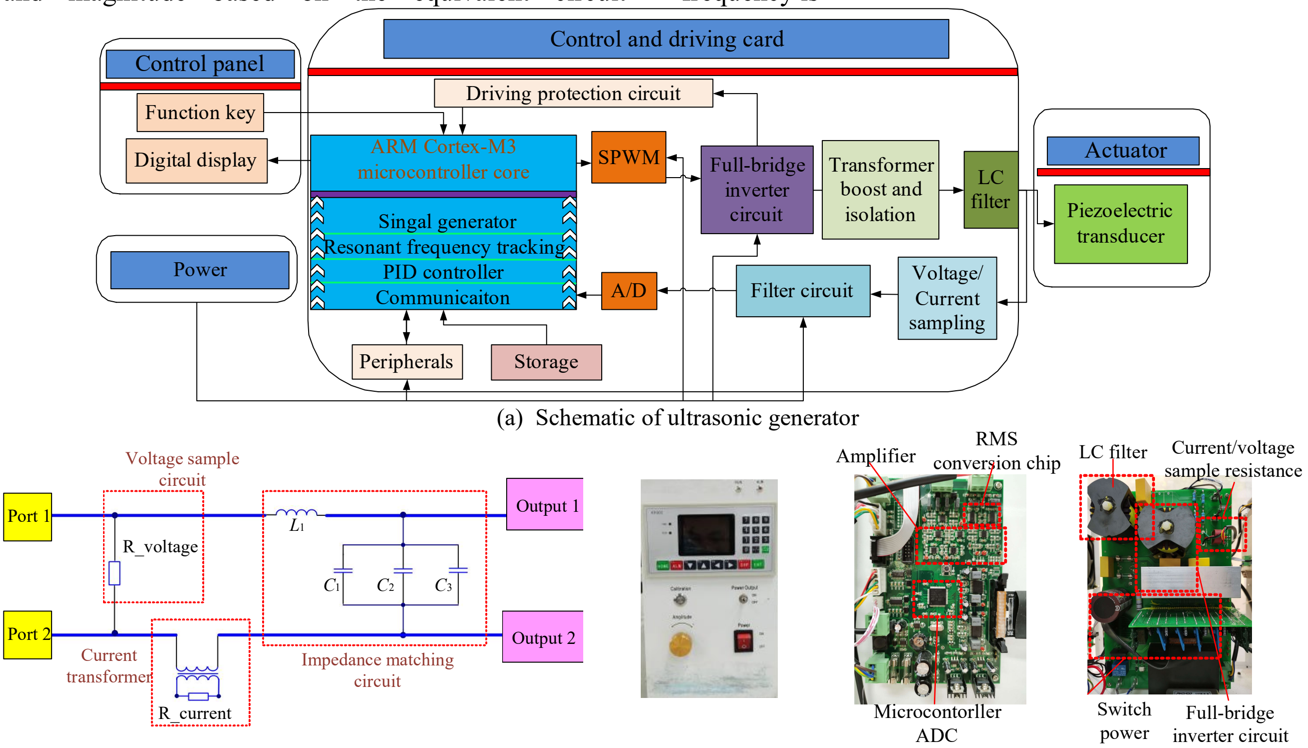

(a) Schematic of ultrasonic generator

(b) Impedance matching and voltage/current sampling circuit for output
(c) Human-machine interaction panel
(d) Control module
(e) Driving module

Fig.6. Hardware of the power ultrasonic system

decreased. The voltage and current of an ultrasonic transducer are sampled by a parallel resistance of 25k ohm and a high frequency pulse current transformer, respectively. Due to the large resistance, the parallel resistance R_voltage do not have a significant impact on the power input and output. Fig.6(c)~(e) shows the hardware of the ultrasonic generator. The switch power module converts the Alternating Current (AC) to Direct Current (DC). The STM32F103 microcontroller generates a PWM signal with an adjustable frequency from 10 kHz to 65 kHz by specified software control. The full-bridge inverter circuit and transformer module amplify the small signal from microcontroller to a high level, and then a sinusoidal signal is generated by a LC filter module to transducer. The driving voltage and sweeping frequency range can be tuned by the function keys so the ultrasonic generator can trigger different types of PT. The signals of voltage and current are transferred to amplifier and voltage/current mean root square (RMS) conversion chip in Fig.6(d). The transformed signal of voltage/current are collected by 12 bits ADC in STM32F103 in sampling rate 1MHz. The theoretical model of amplitude prediction is programmed and implanted in ultrasonic generator. The voltage/current, the frequency and the predicted amplitude are transferred to the LCD for displaying, thus realize the monitoring of voltage, current, resonant frequency and amplitude.

4.2 Validating experiment platform

The experimental setup is presented in Fig. 7, which includes Agilent 4294A impedance analyzer, ultrasonic generator and PTs. Fig.7 (b) shows real-time monitoring interface of LCD including: voltage/current, resonant frequency and amplitude. The vibration amplitude of the tips of the PTs is measured by a Laser Doppler Vibrometer (LDV, Polytech HSV 700 Model), and displayed in a Tektronix MDO3024 Oscilloscope. An infrared thermometer of AS852B (-50°~750°) is used for long time excitation test. The resonant frequency of three PTs is swept by Agilent 4294A impedance analyzer in Fig.7 (a) and the measured results are shown in Fig.8 (a) ~ (c). Then, three PTs are driven by ultrasonic generator in Fig.7 (b) and the driving voltage, current, amplitude, and operating frequency are displayed in Oscilloscope. Especially, to transfer electrical energy to excite the RUM transducer, a couple of wireless magnetic transformer is adopted. In Fig.8 (d) ~ (f), the Channel 1 represents the voltage RMS value; the Channel 2 represents the current RMS value; the Channel 4 represents the amplitude RMS value; the Channel 2 Frequency represents the operating frequency of ultrasonic generator. The data is sampled in a stable state after running for 10 seconds. By the data acquired from oscilloscope, driving voltage and current

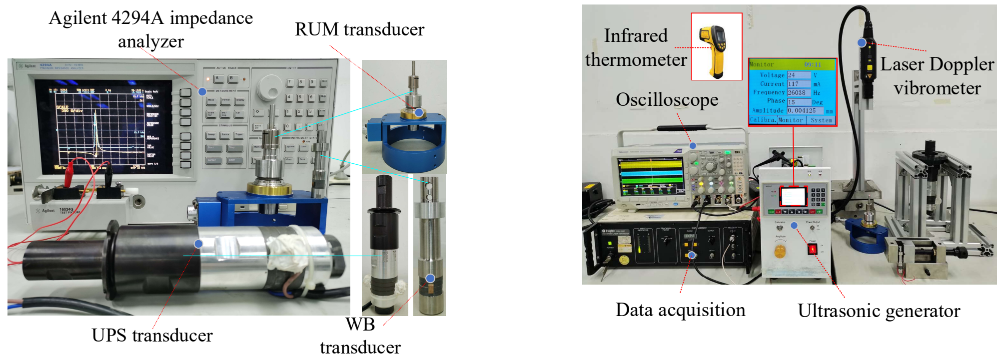

(a) Frequency/impedance measurement (b) Amplitude validating and monitoring platform

Fig.7. Experiment platform for RUM, UPS, WB transducers

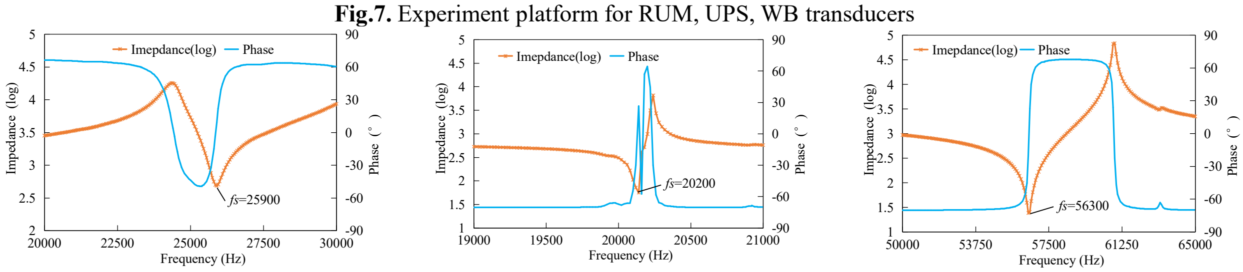

(a) RUM (b) UPS (c) WB

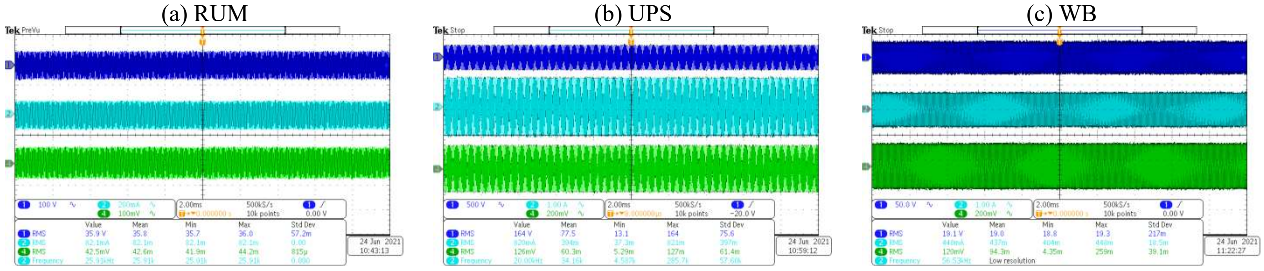

(d) RUM (e) UPS (f) WB

Fig.8. Resonant frequency, current and voltage measurements.

are calibrated and displayed on the LCD in real time as Fig.7 (b). It can be seen that the resonant frequency tracked by ultrasonic generator is consistent with the one swept by Agilent 4294A impedance analyzer in Fig.8. The measured amplitude from LDV displayed on the oscilloscope are calculated with the equation as

$$A\_measured = \frac{10\sqrt{2}A_o}{2\pi f} \tag{21}$$

Where, *A_measured* (μm) is the measured amplitude, A_o (mV) is the data collected from oscilloscope, f (kHz) is the vibration frequency.

4.3 Measurement in idle condition

In experiment, driving voltage, current and frequency are registered to calculate the predicted amplitude *A_predicted*, which is compared to the measured amplitude *A_measured*. Each experiment is repeated three times and the average value is calculated at the steady state after 10s to reduce the thermal influence. It should be noted that as the voltage/current I recorded from experiments is in RMS, 0-peak, peak-peak type, the calculated amplitude is correspondingly attributed to the RMS, 0-peak, peak-peak type. Also, the measurement of voltage/current I, measured amplitude and predicted amplitude discussed in idle condition is in RMS type. Table. 3 shows the measurement of voltage/current, frequency of three transducers. The comparisons of the measured amplitude *A_measured*, the predicted amplitude *A-predicted*, the voltage effect *A_voltage* and the current effect *A_current* are shown in Fig.9. Despite the predicted amplitude of RUM and

WB transducers is higher than the measurement in Fig.9 (a) and (c), the trend of both traces shows a good agreement. This error is due mainly to the dimensional inconsistency of the simulation model and real devices. As a comparison, prediction and measurement of the amplitude of the UPS transducer in Fig.9(b) are matched, with an error less than 5%. The average coefficients of amplitude and current for RUM, UPS and WB transducer from experiments are as $\beta_{RUM'}$ = 0.0361 (μm/mA), $\beta_{UPS'}$ = 0.0209 (μm/mA), $\beta_{WB'}$ = 0.0093 (μm/mA), which are well agreed with the simulation in section 3. Further, in Fig.9, the voltage effect *A_voltage* has no significant influence on the amplitude prediction. Inversely, the current effect *A_current* is consistent with the predicted amplitude *A_measured*. The experimental testing proves that current and resonant frequency are the key factors for amplitude monitoring.

4.4 Measurement under thermal load

The resonant frequency and impedance of ultrasonic transducer are changed due to self-heating effects in a long-time excitation. The cooling method is necessary to avoid frequency and impedance drifting in engineering. However, in order to verify the validity of the amplitude prediction theoretical model, a long-time excitation of thermal load experiment without cooling is conducted. RUM transducer is selected for long time excitation test. An infrared thermometer of AS852B (-50°~750°) is used for temperature measurement. The measuring point is on the flange, which is close to the piezoelectric ceramic. The voltage/current, resonant frequency, temperature, the measured and predicted amplitude are shown in Fig.10. The driving voltage is keeping constantly with feedback control during the experiments. In Fig.10(a)~(c), the RMS driving voltage are 15V, 36V and 91V, respectively. The temperature of ultrasonic transducer is raised with the power consuming increased with a higher driving voltage/current. The temperature increases and then maintains a steady state of self-heating and heat dissipation. Fig.10 (d)~(f) shows the trend of the predicted amplitude *A_predicted*, and the measured amplitude *A_measured* along with temperature variations. The predicted amplitude is come from the mathematic simulation of Fig.5(a). Although there is a difference between the predicted amplitude *A_predicted* and the measured amplitude *A_measured*, the trend of both traces shows a highly agreement and its average errors is less than 10%. Experimental results indicate that the ultrasonic amplitude can still be monitored even if the resonant frequency varies in long-time excitation of self-heating effects.

Table 3
Voltage, current and resonant frequency recorded in experiments.

No.		1	2	3	4	5	6	7	8	9	10	11	12
	U(V)	12	14	16	17	18	21	23	24	25	26	27	30
RUM	*I*(mA)	78	81	85	89	97	102	106	111	118	120	122	125
	f(Hz)	25963	25943	25931	25905	25899	25899	25893	25891	25875	25872	25863	25835
	U(V)	106	110	116	120	126	129	134	140	145	150	157	160
UPS	*I*(mA)	815	845	865	891	903	918	947	972	987	1015	1041	1048
	f(Hz)	20073	20068	20062	20057	20051	20054	20046	20045	20046	20036	20033	20035
	U(V)	10	11	12	13	14	15	16	17	18	19	20	21
WB	*I*(mA)	331	340	362	376	415	424	424	456	454	468	468	511
	f(Hz)	56347	56344	56343	56345	56341	56337	56342	56328	56326	56311	56315	56311

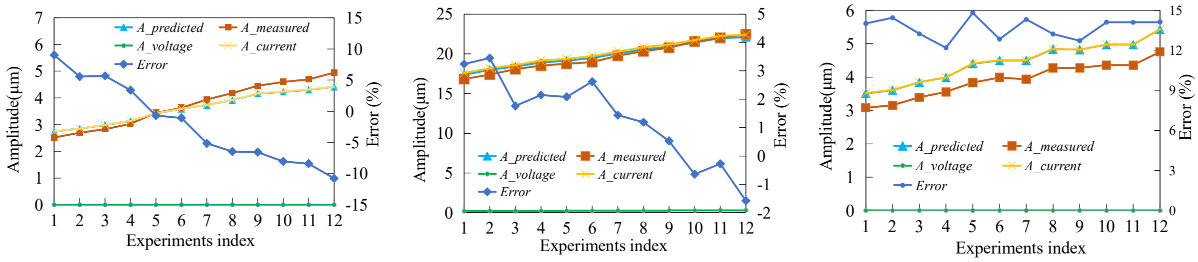

(a) RUM (b) UPS (c) WB

Fig.9. The comparison between the measured and the predicted amplitude.

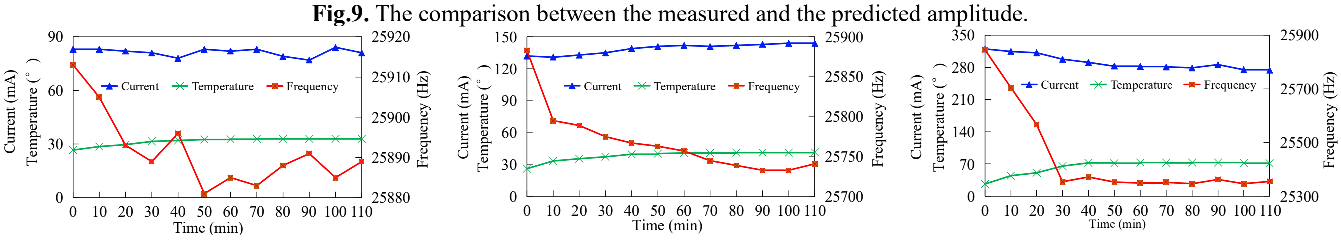

(a) 15V (b) 36V (c) 91V

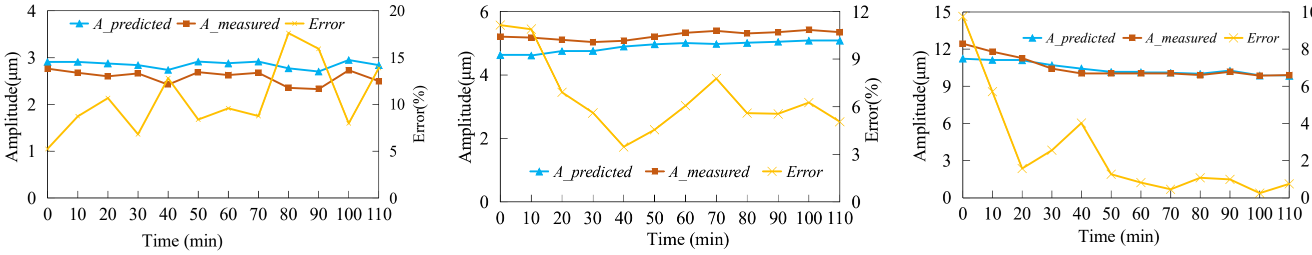

(d) 15V (e) 36V (f) 91V

Fig.10. Comparison between predicted and measured amplitude in excitation time with the temperature effect.

4.4 Measurement under dynamic force load

The schematic and experimental platform of the RUM transducer under force is in Fig. 11. In order to measure the force between the tool tip and workpiece, a force sensor (SBT761A-100kg) is placed between the upper and lower sliders, where the lower slider is in contact with the tool tip and the upper slider is loaded which can be adjusted by tuning the lead screw. The force is recorded by a digital calibrator. The driving strategy is keeping the voltage constantly. In order to reduce the influence of thermal load, a relatively lower RMS driving voltage of 24V (34V in 0-peak type) is selected to ensure that the force plays an essential role in experimental test. The axial force is adjusted by tuning the lead screw. Experimental results are shown in Fig.12. The axial force variation of tool end is in Fig. 12(a). The driving voltage 34 V in 0-peak type remains constantly with or without force, as shown in Fig. 12(b). In Fig. 12(c), the resonant frequency of ultrasonic transducer changed with the increase of force load. By comparing Fig. 12 (d), (e) and (f), the trend of the measured amplitude and the predicted amplitude is consistent with the current variations.

Since the measured amplitude and predicted amplitude curves are a quantity of sampling points, the contour and envelope lines of the measured and predicted amplitude are compared in Fig.13 and Fig.14. It can be seen that the trend of contour of the predicted and measured amplitude in Fig.13 (a), (b) shows highly agreement. Although the error between the predicted and measured amplitude is fluctuating, the average error of top contour is less than 15%, and the one of bottom contour is less than 10%. In order to evaluate the overall error level of the predicted and the measured amplitude, fourth order polynomial fitting is carried out on the top and bottom contour as follows:

$$y_{T\_predicted}(x) = -8.176\times10^{-20}x^4 + 2.4813\times10^{-14}x^3 -1.9304\times10^{-9}x^2 + 7.81182\times10^{-6}x + 4.32848 \tag{22}$$

$$y_{T\_measured}(x) = -2.10855\times10^{-19}x^4 + 5.60225\times10^{-14}x^3 -3.9537\times10^{-9}x^2 + 3.55367\times10^{-5}x + 4.57912 \tag{23}$$

$$y_{B\_predicted}(x) = 3.54138\times10^{-20}x^4 - 2.12809\times10^{-14}x^3 +1.87616\times10^{-9}x^2 - 5.40908\times10^{-6}x - 4.34485 \tag{24}$$

$$y_{B\_measured}(x) = 4.87934\times10^{-19}x^4 - 8.74664\times10^{-14}x^3 +4.87936\times10^{-9}x^2 - 4.44749\times10^{-5}x - 4.28313 \tag{25}$$

Where, $y_{T\_predicted}$, $y_{T\_measured}$ are top envelop fitting functions of predicted and measured amplitude; $y_{B\_predicted}$, $y_{B\_measured}$ are bottom envelop fitting function of the predicted and measured amplitude; x=65535/200t is the point position sampled; t is the time. The fitted line and error are shown in Fig.14(a), (b). From the

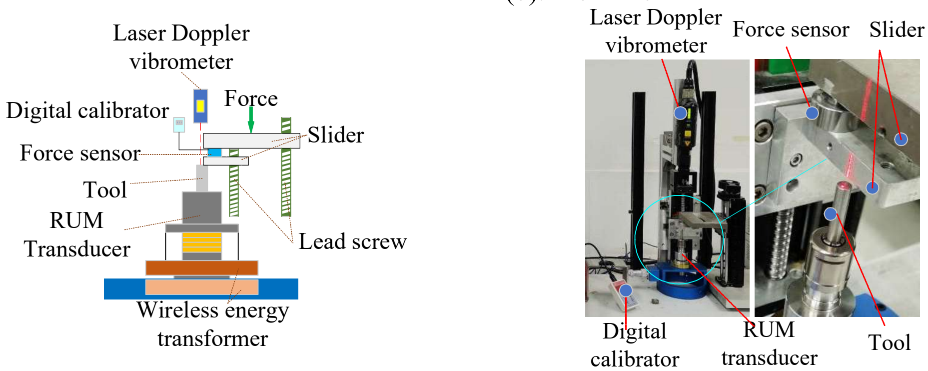

(a) Schematic (b) Experimental platform

Fig.11. Amplitude measurement to the transducer in force load.

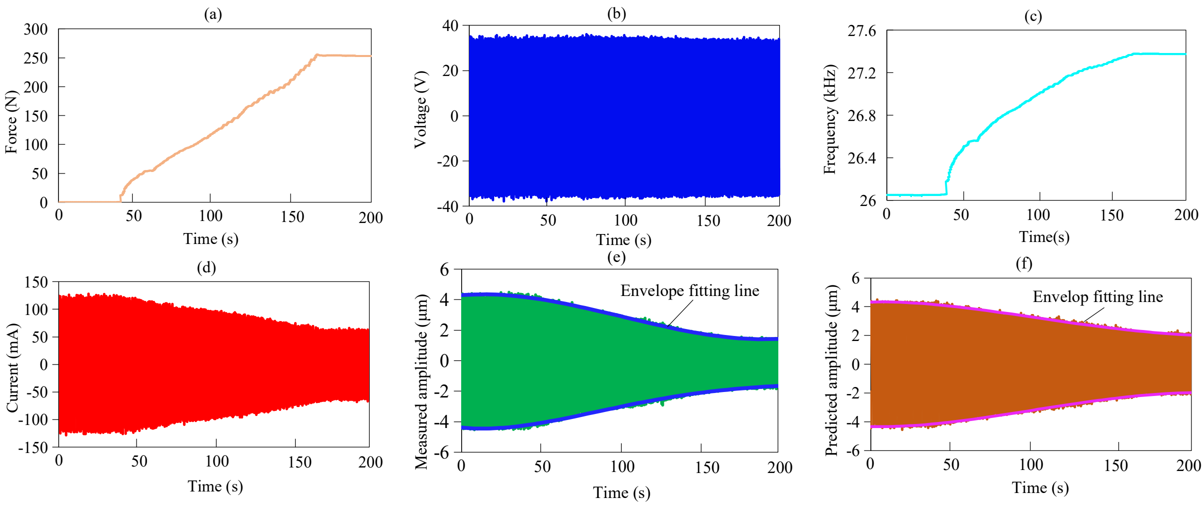

Fig. 12. Comparison between the predicted and measured amplitude in force load:(a) Force, (b) Voltage, (d) Frequency, (d) Current, (e) Measured amplitude, (f) Predicted amplitude.

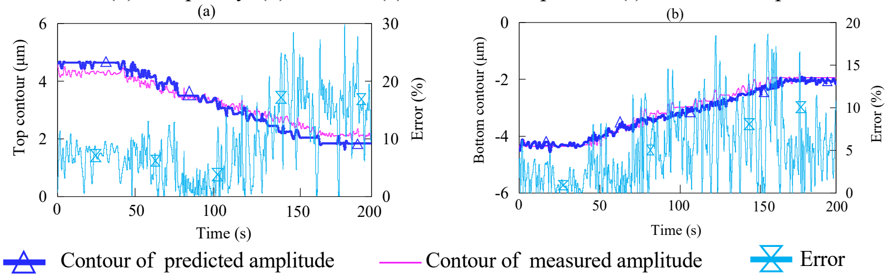

Fig.13. The contour comparison for the predicted and measured amplitude:(a) top contour; (b) bottom contour.

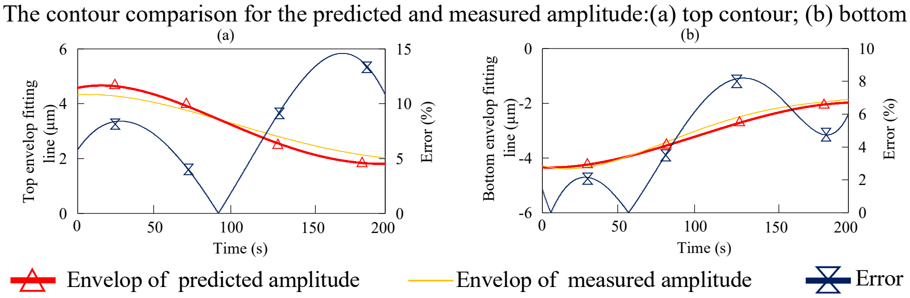

Fig.14. The comparison of envelop between the predicted and measured amplitude:(a) top envelop; (b) bottom envelop.

simulation of fitting line, the average error between the predicted and measured amplitude of top envelop fitting lines is less than 10% in Fig.14(a); the average error between the predicted and measured amplitude of bottom envelop fitting lines is less than 6% in Fig.14(b). Therefore, the experiment results show that the proposed model is effective in predicting ultrasonic amplitude of PT in force load.

5 Conclusions

In this study, a novel real-time and low-cost strategy for monitoring the ultrasonic amplitude of piezoelectric transducer is presented. It is proved that if the current and operating resonant frequency are collected in real time, the amplitude of PTs can be predicted. Based on the piezoelectric equations of PZT stack and the wave equation of a solid horn, the dynamic displacement expression is deduced and combined with displacement transmission matrix. The amplitude prediction model of the PTs is established based on the current and resonant frequency. Amplitude prediction simulation is involved with voltage/current and frequency. The proposed model is programmed and implanted in ultrasonic generator and an automated monitoring platform for amplitude measurement is realized. Three types of RUM, UPS and WB PTs are adopted in the verification experiments. In addition, a long-time excitation of thermal effects and force load applied experiments are conducted on the RUM PT. Validating experiments show that the predicted amplitude in simulation is consistent with the measured amplitude, even under the conditions of thermal effect and force load.

CRediT authorship contribution statement

Heng Zhao: Methodology, Conceptualization, Hardware structure, Software-program, Validation, Investigation, Data curation, Writing original draft, Review & editing. Jianzhong Ju: Data curation, Review & editing. Shuyuan Ye: Hardware structure, Software-program, Data curation, Review & editing. Xuan Li: Conceptualization, Review & editing. Zhili Long: Supervision, Conceptualization, Hardware structures, Review & editing, Project administration, Funding acquisition.

Declaration of Competing Interest

The authors declare that they have no known competing financial interests or personal relationships that could have appeared to influence the work reported in this paper.

Acknowledgments

This work is supported by the Key Research and Development Program of Guangdong Province (2020B090926001), National Natural Science Foundation of China (U1913215, U1713206), and Basic Research Plan of Shenzhen (JCYJ20200109113429208, JCYJ20200109112803851, GJHZ20180928154402130) for the financial support. Meanwhile, the authors would like to appreciate the anonymous reviewers and the editor for their valuable comments.

References

[1] X. Zhu, B. lin, L. Liu, Y. Luan, Power transfer performance and cutting force effects of contactless energy transfer system for rotary ultrasonic grinding, IEEE Trans. Ind. Electron. 63 (5) (2016)2785-2795.

[2] F. Ning, W. Cong, H. Wang, Y. Hu, Z. Hu, Surface grinding of CFRP composites with rotary ultrasonic machining: a mechanistic model on cutting force in the feed direction, Int. J. Adv. Manuf. Technol. 92 (1) (2017)1217-1229.

[3] C. Huang, M. Zhou, H. Zhang, A cutting force prediction model in axial ultrasonic vibration end grinding for BK7 optical glass considering protrusion height of abrasive grits, Measurement. 180(2021)109512.

[4] Y. Wang, B. Lin, S. Wang, X. Cao, Study on the system matching of ultrasonic vibration assisted grinding for hard and brittle materials processing. Int. J. Adv. Manuf. Technol. 77(2014)66-73.

[5] A. Jain, G. Singh, V. Jain, D. Gupta, Feasibility analysis for machining serpentine microchannels on glass using rotary ultrasonic milling, Measurement. 160(2020)107844.

[6] P. Kang, D. Wang, Study on the performances of the drilling process of nickel-based superalloy Inconel 718 with differently micro-textured drilling tools, Int. J. Mech. Sci. 180(2020)105658.

[7] M Baraheni, A Saeid, Mathematical model to predict cutting force in rotary ultrasonic assisted end grinding of Si3N4 considering both ductile and brittle deformation, Measurement. 160(2020)107586.

[8] J. Zhu, Y. Tian, C. Yang, Cui L, Wang F. Low-cost and fast fabrication of the ultrasonic embossing on the polyethylene terephthalate (PET) films using laser processed molds, Microsyst. Technol. 23 (12) (2017)5653-5668.

[9] F. Wang, X. Zhao, D. Zhang, Y,Wu. Development of novel ultrasonic transducers for microelectronics packaging, J. Mater. Process. Technol. 209 (3) (2009)1291-1301.

[10] F. Wang, H. Zhang, C. Liang, Y. Tian, X Zhao, Design of high-frequency ultrasonic transducers with flexure decoupling flanges for thermosonic bonding, IEEE Trans. Ind. Electron. 63 (4) (2015)2304-2312.

[11] H. Zhang, J. Zhao, Y. Hou, J. Zhang, J. Huang, A new method to enhance the tip vibration amplitude output of the high frequency piezoelectric ultrasonic transducer used in the thermosonic bonding, Sens. Actuator A-Phys. 294(2019)116-125.

[12] Z. Long, J. Zhang, X. Wu, Y Liu, Y. Zhou X, Impedance modeling of ultrasonic transducers used in heavy aluminum wire bonding, IEEE Trans. Compon. Pack. Manuf. Technol. 8 (6) (2018) 1107-1115.

[13] S. Lin, H. Guo, J. Xu, Actively adjustable step-type ultrasonic horns in longitudinal vibration, J. Sound Vibr. 419(2018)367-379.

[14] C. Guang, C. Ren, Y. Zou, X. Qin, L. Lu, Mechanism for material removal in ultrasonic vibration helical milling of Ti6Al4V alloy, Int. J. Mach. Tools Manuf. 138(2019)1-13.

[15] X. Xiao, K. Zheng, W Liao, Theoretical model for cutting force in rotary ultrasonic milling of dental zirconia ceramics, Int. J. Adv. Manuf. Technol. 75 (9-12) (2014)1263-1277.

[16] X. Jiang, K. Wang, R. Shao, J. K.Mills. D. Zhang, Self-compensation theory and design of contactless energy transfer and vibration system for rotary ultrasonic machining, IEEE Trans. Power Electron. 33 (10) (2017)8650-8660.

[17] Z. Liu, Y. Jin, P. Bian, Study on influence of load on characteristics of ultrasonic machining acoustic system, Aviation Precision Manufacturing Technology. 1(2012)10-13.

[18] S. Zhao, S. Li, W. Guo, C. Zhang, B. Cong, Quantitative diagnosis method of beam defects based on laser Doppler non-contact random vibration measurement, Measurement. 152(2019)107271.

[19] H. Zhou, J. Zhang, P. Feng, D. Yu, Z. Wu, An amplitude prediction model for a giant magnetostrictive ultrasonic transducer, Ultrasonics. 108(2020)106017.

[20] H. Zhou, J. Zhang, P. Feng, D. Yu, W. Cai, An output amplitude model of a giant magnetostrictive rotary ultrasonic machining system considering load effect, Precision Engineering. 60(2019)340-347.

[21] H. Gaul, A. Shah, M. Mayer, Y. Zhou, The ultrasonic wedge/wedge bonding process investigated using in situ real-time amplitudes from laser vibrometer and integrated force sensor, Microelectron. Eng. 87 (4) (2010)537-542.

[22] W. Cong, Z. Pei, N. Mohanty, E. Van Vleet, C. Treadwell, Ultrasonic vibration amplitude in rotary ultrasonic machining: a novel measurement method and effects of process variables, J. Manuf. Sci. Eng.-Trans. ASME 133 (3) (2011)1-6.

[23] M Moghaddas, K. Graff, On the effect of load on vibration amplitude in ultrasonic-assisted drilling, The International Int. J. Adv. Manuf. Technol. 106 (7) (2020)3081-3094.

[24] S. Saffar, A. Abdullah, Vibration amplitude and induced temperature limitation of high power air-borne ultrasonic transducers, Ultrasonics. 54 (1) (2014)168-76.

[25] S. Saffar, Amir. Saffar, Simple method for measuring vibration amplitude of high power airborne ultrasonic transducer: Using thermo-couple, Ultrasonics. 54 (3) (2014)821-825.

[26] F. Ning, H. Wang, W. Cong, P. Fernando, A mechanistic ultrasonic vibration amplitude model during rotary ultrasonic machining of CFRP composites, Ultrasonics. 76(2017)44-51.

[27] S. Voronina, V. Babitsky, Autoresonant control strategies of loaded ultrasonic transducer for machining applications, J. Sound Vibr. 313 (3-5) (2008)395-417.

[28] M. Karafi, K. Farshad, Evaluation of mechanical and electric power losses in a typical piezoelectric ultrasonic

transducer, Sens. Actuator A-Phys. 288(2019)156-164.

[29] B. Zhao, B. Chang, L. Yuan, P. Li, Influence of force load on the stability of ultrasonic longitudinal-torsional composite drilling system, Int. J. Adv. Manuf. Technol. 106 (3) (2020)891-905.

[30] S. Lin, Principle and design of ultrasonic transducer, Scie Pre. 3 (2006).

[31] L. Joseph. Rose, Ultrasonic Wave in Solid Media, Cambridge University Press. 2004.

[32] M. Karafi, S. Kamali, A continuum electro-mechanical model of ultrasonic Langevin transducers to study its frequency response, Appl. Math. Model, 92(2021)44-62.

[33] A. Abdullah, M. Shahini, P. Abbas, An approach to design a high power piezoelectric ultrasonic transducer, J. Electroceram. 22 (4) (2009)369-382.

[34] K. Vladimir, A. Kirill. Pichugin, X. Li, A. Meadows, V. Babitsky, Resonant Tuning of Langevin Transducers for Ultrasonically Assisted Machining Applications, IEEE Trans, IEEE Trans. Ultrason. Ferroelectr. Freq. Control. 67 (9) (2020)1888-1896.

[35] H. Zhao, S. Ye, J. Ju, Zi. Long, Y. Yang, Z. Long, A Novel Heat Shrinkable Ultrasonic Transducer for Rotary Ultrasonic Micro-Nano Precision Manufacturing, IEEE Access. 99 (2021).

[36] H. Zhang, F. Wang, D. Zhang, L. Wang, X. Tao, A new automatic resonance frequency tracking method for piezoelectric ultrasonic transducers used in thermosonic wire bonding, Sens. Actuator A-Phys. 235(2015) 140-150.

[37] Z. Long, J Zhang, C Wang, H Zhao, Y Li, Compensation modeling and optimization on contactless rotary transformer in rotary ultrasonic machining, J. Manuf. Sci. Eng.-Trans. ASME. 142(10) (2020)1-11.

[38] Z Long, J. Zhang, Q. Gao, H. Zhao, Y. Li, Novel Double Compensation for Impedance-Frequency Characteristics of Rotary Ultrasonic Machining via Multiobjective Genetic Algorithm, IEEE Trans. Autom. Sci. Eng. (2020)1-11.